RESEARCH ARTICLE

Key Points:
- Tropical Pacific wind-driven ocean circulation intensified transitioning to hiatus
- Decadal anomalies of SST and ocean circulation display strong seasonality
- Seasonality due to variations in wind stress and zonal temperature advection

Correspondence to:
D. J. Amaya,
djamaya@ucsd.edu

Seasonality of tropical Pacific decadal trends associated with the 21st century global warming hiatus

Dillon J. Amaya[1], Shang-Ping Xie[1], Arthur J. Miller[1], and Michael J. McPhaden[2]

[1]Scripps Institution of Oceanography, University of California, San Diego, California, USA, [2]NOAA/Pacific Marine Environmental Laboratory, Seattle, Washington, USA

Abstract Equatorial Pacific changes during the transition from a nonhiatus period (pre-1999) to the present global warming hiatus period (post-1999) are identified using a combination of reanalysis and observed data sets. Results show increased surface wind forcing has excited significant changes in wind-driven circulation. Over the last two decades, the core of the Equatorial Undercurrent intensified at a rate of 6.9 cm s^{-1} decade^{-1}. Similarly, equatorial upwelling associated with the shallow meridional overturning circulation increased at a rate of 2.0×10^{-4} cm s^{-1} decade^{-1} in the central Pacific. Further, a seasonal dependence is identified in the sea surface temperature trends and in subsurface dynamics. Seasonal variations are evident in reversals of equatorial surface flow trends, changes in subsurface circulation, and seasonal deepening/shoaling of the thermocline. Anomalous westward surface flow drives cold-water zonal advection from November to February, leading to surface cooling from December through May. Conversely, eastward surface current anomalies in June–July drive warm-water zonal advection producing surface warming from July to November. An improved dynamical understanding of how the tropical Pacific Ocean responds during transitions into hiatus events, including its seasonal structure, may help to improve future predictability of decadal climate variations.

1. Introduction

Global average surface air temperature (SAT) has been significantly increasing since the industrial revolution [*Hartmann et al.*, 2013], although this overall global warming trend has been punctuated by periods of weaker/stalled warming or cooling. Sometimes lasting several decades, breaks in 20th century warming have been called global warming "hiatuses" in the literature [e.g., *Meehl et al.*, 2011; *Kosaka and Xie*, 2013; *England et al.*, 2014]. This has reignited debate on the validity of anthropogenic climate change among skeptics and confusion among the public.

Examples of hiatuses include a period of time from the 1940s to the 1970s and currently from about 2000 to the present (Figure 1a). In particular, the current global warming hiatus has been the subject of significant scientific scrutiny. For example, a growing body of literature has shown increased ocean heat uptake over the last decade [*Meehl et al.*, 2011; *Katsman and van Oldenborgh*, 2011; *Meehl et al.*, 2013; *Guemas et al.*, 2013]. Yet uncertainty remains on the mechanisms driving the transition from a nonhiatus period to a global warming hiatus period [*Solomon et al.*, 2010, 2011; *Kaufmann et al.*, 2011]. Since future hiatus periods are likely to disrupt future warming trends [*Easterling and Wehner*, 2009; *Hansen et al.*, 2011], it is important to ascertain the impact that a hiatus has on the global climate system.

Recent research has focused on the Pacific Ocean as a potential player in modulating global warming trends due to its immense volume [*Meehl et al.*, 2011; *Brown et al.*, 2015; *Dai et al.*, 2015]. Specifically, studies have shown periods of hiatus correspond well with negative phases of the Pacific Decadal Oscillation (PDO) [*Meehl et al.*, 2011; *Kosaka and Xie*, 2013; *England et al*, 2014], an internal mode of climate variability [*Mantua et al.*, 1997; *Power et al.*, 1999; *Folland et al.*, 2002]. During a negative (positive) phase, this ENSO-like pattern of climate variability is characterized by cooler (warmer) tropical Pacific sea surface temperatures (SST) and stronger (weaker) trade winds. The 1990s saw the beginning of an easterly trend in the trade winds and as a result the first decade of the 21st century has been dominated by anomalously intense trades, which are normally associated with a negative PDO (Figures 1b and 1c).

A growing body of research has indicated that a negative phase PDO, which has significant impacts on tropical Pacific SST, heat content, and atmospheric/ocean circulations, forces regional climate anomalies in
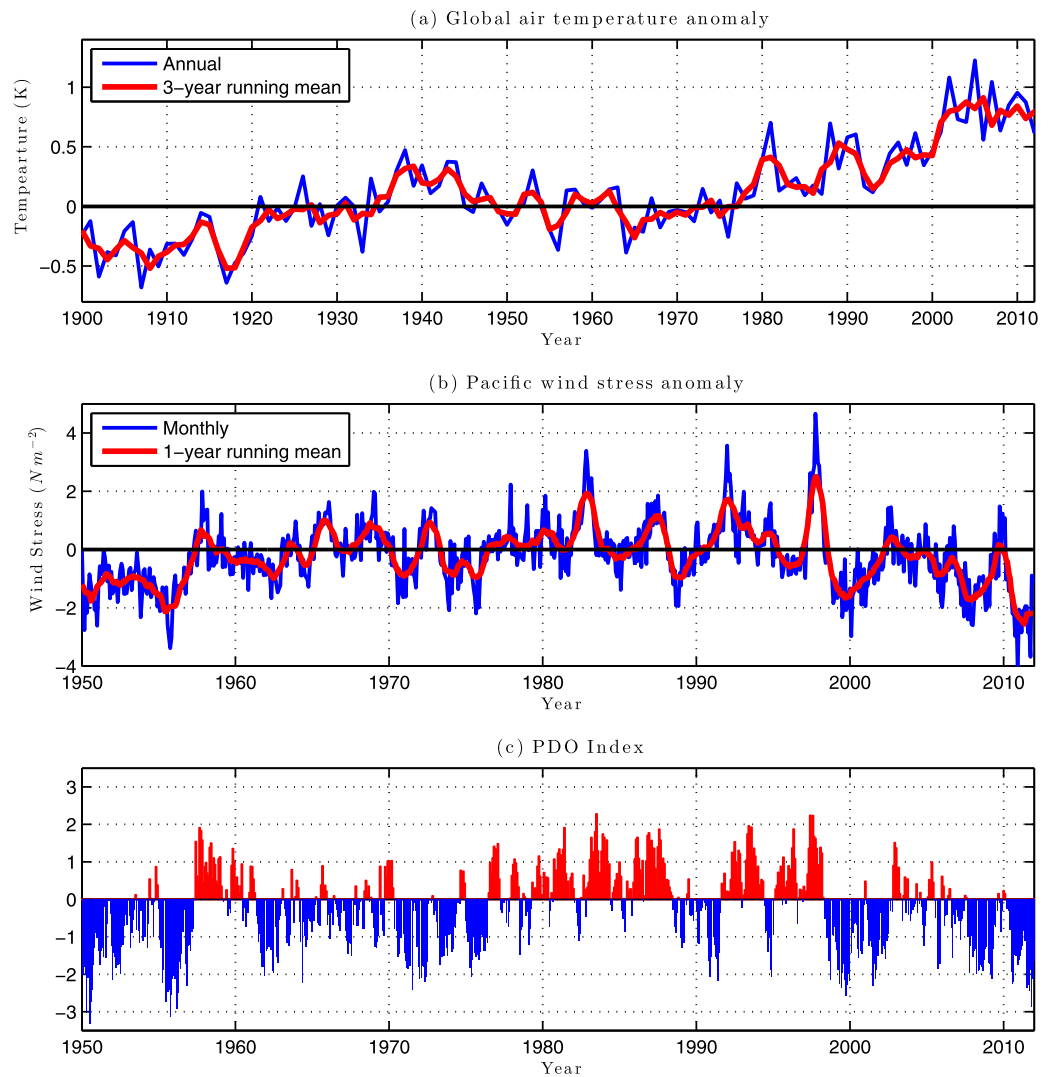
Figure 1. GISS global-averaged surface air temperature anomalies (a), zonal wind stress anomalies averaged 5°S–5°N, 180°–150°W (b), and the Pacific Decadal Oscillation (PDO) Index (c). (top) From January 1900 to December 2011, while both (b) and (c) from January 1948 to December 2011. Blue time series are annual (Figure 1a), monthly (Figure 1b), and negative (Figure 1c) data. Red time series are 3 (Figure 1a) and 1 year (Figure 1b) running means and positive PDO values (Figure 1c). Wind stress anomalies were scaled by 100.

North America, and is a contributing mechanism to the current global warming hiatus [e.g., *Kosaka and Xie*, 2013; *England et al.*, 2014; *McGregor et al.*, 2014]. It remains largely unclear though how the eastern Pacific has remained cool even with increased global radiative forcing.

England et al. [2014] describe an intensification of wind-driven circulation in the tropical Pacific during the hiatus, which would drive increased equatorial upwelling in the central and eastern Pacific, thus sustaining cool SSTs. Additionally, *Kosaka and Xie* [2013] and *Trenberth et al.* [2014] show a seasonal dependence in surface variables associated with global "hiatus modes." Here, we focus on the seasonal response of surface climate anomalies and subsurface ocean circulation anomalies in the tropical Pacific to increased wind stress forcing associated with a PDO phase transition into a hiatus period.

Thanks to satellite altimetry, the Argo program, and the Tropical Atmosphere Ocean/Triangle Trans-Ocean Buoy Network (TAO/TRITON) moored buoys in the tropical Pacific, the most recent PDO phase change is perhaps the best-observed decadal climate shift in history. This study utilizes extensive ocean reanalysis and observational data sets to bring further clarity to how tropical Pacific Ocean circulation has responded to strengthening trade winds, how these changes maintain cool SSTs at the surface, and how these responses vary seasonally. Understanding the seasonal variability of the circulation is critical in determining

the role the Pacific Ocean plays in the current hiatus and would improve predictability of future events. Our analysis aims to shed light on the interplay between surface and subsurface variability in the tropical Pacific Ocean during the period 1990–2009.

In the following section, we outline the reanalysis products and observational data used in this study. We then present our results illustrating how tropical Pacific surface and subsurface anomalies have changed in the last two decades. An analysis into the seasonal cycle of these phenomena is then performed, followed by a summary and discussion of our results in the context of tropical Pacific climate variability and the current global warming hiatus.

2. Data and Methods

### 2.1. Reanalysis Products and Observational Data

In the past decade, there has been a growing interest in using ocean syntheses (model dynamics coupled with sparse observational data to produce a complete ocean description) to improve our understanding of decadal climate variability and our ability to predict climate on decadal time scales [e.g., *Smith et al.*, 2007; *Keenlyside et al.*, 2008; *Pohlmann et al.*, 2009; *Köhl*, 2014]. Of the variety of methods utilized to assimilate observed data into global ocean models, the adjoint method provides a description of the ocean circulation that exactly obeys the model equations for dynamical principles [*Wunsch and Heimbach*, 2006]. Reanalysis products that employ this assimilation method are therefore valuable for research in the dynamics of decadal climate variability.

We use the second German contribution to Estimating the Circulation and Climate of the Ocean system (GECCO2), a reanalysis product that runs from 1948 to 2011 (iteration 28) and is based on the Massachusetts Institute of Technology general circulation model [*Marshall et al.*, 1997]. This reanalysis product utilizes a 4D-var, adjoint method of data assimilation that improves upon its predecessor (GECCO) by featuring higher horizontal and vertical resolution and additional physics [*Köhl*, 2014]. GECCO2 was forced twice per day by the National Center for Environmental Prediction climatology for the entire run. Additionally, satellite measured monthly mean wind stress fields were included beginning in the early 1990's [*Köhl and Stammer*, 2008]. The native output grid is 1/3° with meridional refinement near the equator and 1° zonal spacing; however, the data have been linearly interpolated to a 1° × 1° for ease in processing. All figures derived from the GECCO2 data use this interpolated grid with the exception of Figure 8. We use GECCO2 products for SST, sea surface height (SSH), and zonal and meridional components of wind stress/currents. Model heat budget terms for GECCO2 were not saved or made available to the public. Therefore, we estimated zonal temperature advection using finite differencing of monthly means. Additionally, SAT was taken from the Goddard Institute for Space Studies Temperature Analysis (GISSTEMP) [*Hansen et al.*, 2006, 2010]. GISSTEMP is available from 1880-present and uses the base period 1951–1980 to calculate anomalies. Finally, the PDO Index was taken from the National Climatic Data Center, which is available from 1854 to present.

To determine the robustness of our findings, we compared all GECCO2-derived results with National Oceanic and Atmospheric Administration's Extended Reconstructed Sea Surface Temperatures Version 3b (ERSST), which is available on a 2° × 2° grid from 1854 to present [*Smith et al.*, 2008]. We also compared our findings with SST, zonal wind stress, and ADCP zonal current velocity observations taken by the TAO/TRITON moorings at 5°S–5°N, 147°E–95°W [*McPhaden et al.*, 1998]. It is important to note that TAO/TRITON temperature profiles were among the observational data sets assimilated into GECCO2 [*Köhl and Stammer*, 2008]; however, a 30 year 4D-var assimilation may not necessarily reproduce SST accurately. Therefore, we include our results using TAO/TRITON measurements. In our comparisons, GECCO2 data were resampled to be temporally and spatially consistent with a given TAO/TRITON product. With the exception of Figure 1a, all figures were generated using GECCO2 data unless otherwise specified in the figure title.

2.2. Trend Analysis

Our analysis period for this study is from January 1990 to December 2009. All anomalies and trends are calculated for GECCO2 variables relative to the 1980–2009 climatology. To estimate trends in our data, we use a simple linear regression technique. In section 3.1, we report the slope of the linear fit for the 20 year analysis period at each grid point in units per decade (Figures 2, 4 insert, 5b, 6b, and 6d). In section 3.2, time/longitude plots are generated by linearly regressing a time series of each calendar month over the 20 year period (i.e., collect all Januaries from 1990 to 2009 and linearly regress). The slope of the linear fit is then
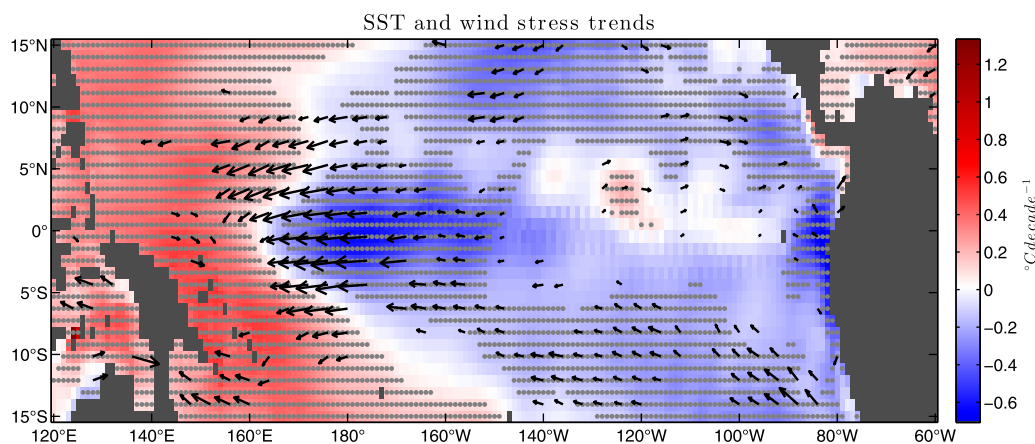
Figure 2. Trends in SST (°C decade^{-1}) and surface wind stress (N m^{-2} decade^{-1}) during 1990–2009. Stippling indicates SST trend significance at the 95% level. Wind stress vectors are only plotted where significant at the 95% level. The maximum wind stress trend vector represents 0.02 N m^{-2} decade^{-1}.

reported for each calendar month at each longitude (Figures 7, 8, 11, and 12). In these figures, we limit trends in surface wind stress and surface currents to only the zonal component because it dominates the overall trend in the vector fields (not shown).

Seasonal subsurface trends in temperature and current velocities are calculated by collecting all occurrences of December–March and July–November and linearly regressing from 1990 to 2009. The slopes are then reported for each depth, latitude/longitude (Figures 9 and 10). Statistical significance for trends was determined using the Mann-Kendall test [*Kendall*, 1975], which tests the null hypothesis of trend absence in a time series against the alternative of trend. The Mann-Kendall test has the added benefit of being less affected by outliers sometimes contained in observations. If a Student's *t* test is applied to the same data, our results do not change.

3. Results

3.1. Surface and Subsurface Trends

Figure 1a shows SAT anomalies averaged globally, while Figure 1b depicts area-averaged zonal wind stress anomalies in the equatorial Pacific Ocean. Although there is an overall warming trend in SAT anomalies, there are two major periods of hiatus from about 1940 to the mid-1970s and from about 2000 to the present. Interestingly, the former exhibits a slight cooling trend from 1940 to 1970 while the latter is associated with no apparent trend. When compared to Figure 1b, the most recent hiatus corresponds closely to a general strengthening of easterly wind anomalies in the equatorial Pacific. This easterly trend seems to begin well before the present hiatus period sometime around 1993. Conversely, the 1940–1970 hiatus is characterized by a general westerly trend in the wind stress that extends from about 1950–1970.

It is therefore apparent that not only do the two hiatuses described above exhibit slightly different SAT trends, they also occur during opposite trends in equatorial Pacific wind stress. While the slowdown of radiative forcing is an important cause of the 1940s–1970s warming hiatus [e.g., *Solomon et al.*, 2011], the PDO plays an important role in the current hiatus [*Marotzke and Forster*, 2015]. Determining the mechanisms that drive the different SAT characteristics of hiatus periods is a complicated matter involving globally coupled ocean-atmosphere interactions and is an active area of research beyond the scope of this study. The background trends in the wind stress, however, correlate well with PDO phase transitions in the mid-to-late 1970s and again in the mid-to-late 1990s. By correlating the PDO Index with the zonal wind stress time series, we get a correlation coefficient of 0.48. Thus, strong easterly winds and periods of hiatus tend to be associated with negative phases of the PDO, which is consistent with previous studies [e.g., *Kosaka and Xie*, 2013; *England et al.*, 2014]. The remainder of the results will attempt to describe the 1990s PDO phase transition from a nonhiatus (positive PDO) period into the resulting hiatus (negative PDO) period in the context of this background strengthening of easterly wind stress and the resulting impact on the equatorial Pacific surface and subsurface.
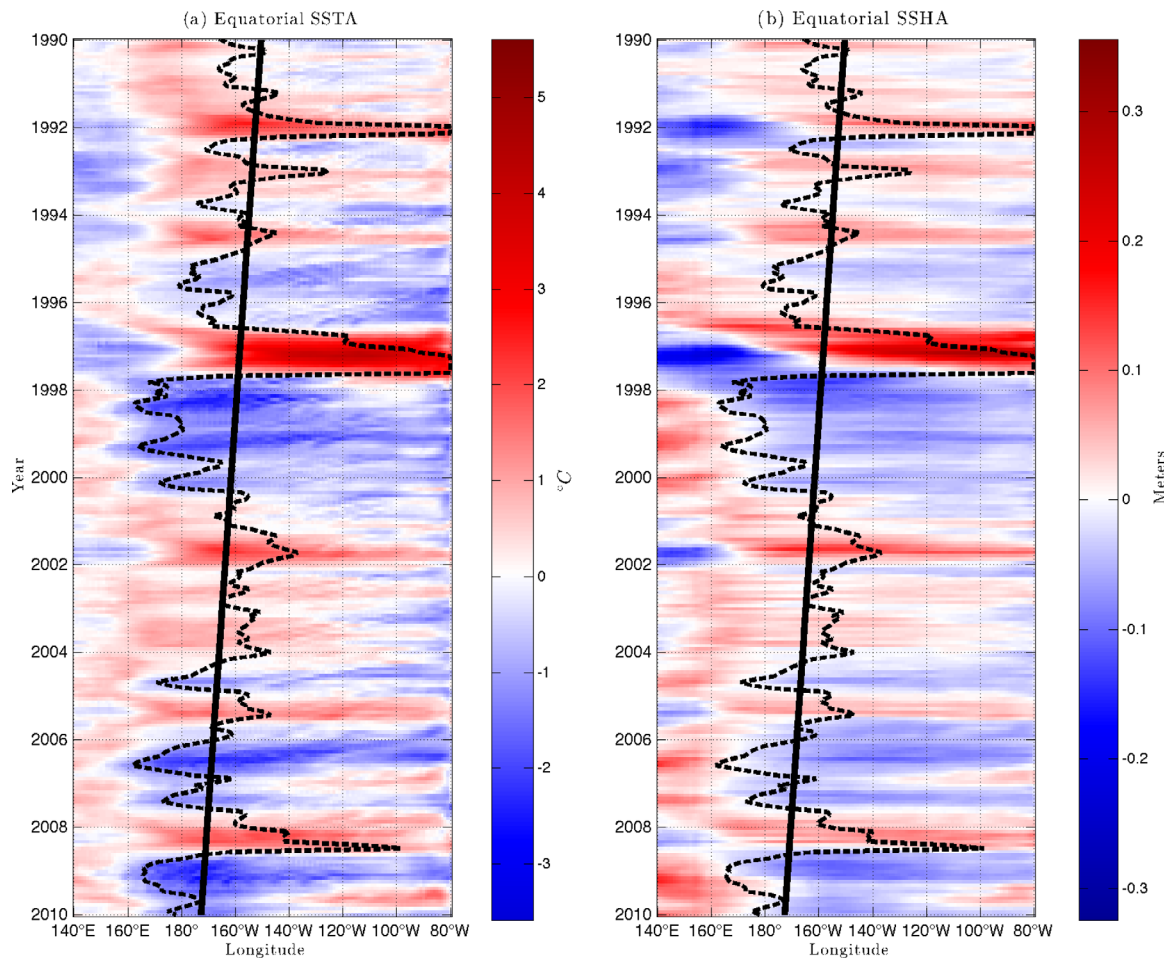
Figure 3. Time/longitude plots of SST anomalies (a) and SSH anomalies (b) averaged over 5°S–5°N. The dashed lines outline the 27.5°C isotherm. The line of best fit is in solid black.

Figure 2 depicts the 1990–2009 trends in SST and surface wind stress in the tropical Pacific. Stippling indicates the SST trend is significant at the 95% for a Mann-Kendall test. The wind stress trend vector is only plotted where the zonal and meridional component are both statistically significant at 95%. As anticipated by Figure 1b, there are easterly trends throughout much of the central tropical Pacific associated with a phase transition from a positive PDO in the 1990s to a negative PDO in the 2000s. Similarly, the SST trends reflect this phase transition with largely negative trends along the equatorial strip.

Figure 3a shows how the Pacific cold-tongue has varied during the transition to the present hiatus period. This is accomplished by averaging monthly SST anomalies 5°S–5°N over the basin from 1990 to 2010 and plotting them as a time/longitude plot. Over this time period, the edge of the equatorial cold-tongue (outlined by the 27.5°C isotherm) has shifted westward by 20.2° longitude in response to the increased zonal wind stress, which is significant at 99% for a Mann-Kendall test (Figure 3a). Intensified trade winds would lead to an anomalous build up of SSH in the west equatorial Pacific warm pool region (Figure 3b) [e.g., *Merrifield et al.*, 2012]. The SSH build up is associated with a deepened thermocline. We estimated the depth of the thermocline as the depth of the 20°C isotherm and averaged over 5°S–5°N, 140°E–180°W (Figure 4, purple box). A monthly time series of this area average shows the thermocline has been anomalously depressed over the west equatorial Pacific by 22.8 m over the 20 year period as estimated by linear regression. Averaging over 5°S–5°N, 170°W–130°W in the central basin (Figure 4, red box), there is an anomalous shoaling of less than a meter over the 20 year period. While the thermocline shoaling in the central Pacific is not significant, the thermocline deepening in the western is significant at 99%. We then use the zonal gradient in the depth of the thermocline to estimate the zonal subsurface pressure gradient along the western and central equatorial strip. By taking the difference of the purple box and the red box in Figure 4, we show an upward trend in the zonal gradient that is significant at 99% for a Mann-Kendall test. This would suggest
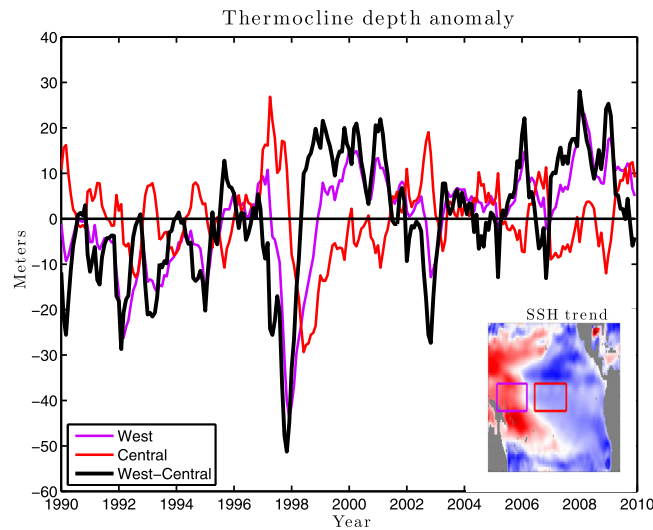
Figure 4. Time series for the depth of the 20°C isotherm averaged from 5°S–5°N, 140°E–180°W (purple box/line), 5°S–5°N, and 170°W–130°W (red box/line). The difference of the red box from the purple box is shown in black. Positive (negative) anomalies represent a deeper (shallower) thermocline. The insert shows the SSH trend.

that even though the shoaling trend in the central Pacific is small, the deepening in the western Pacific is strong enough to significantly intensify the zonal subsurface pressure gradient. Similar trends are evident in the 20°C depth based only on observations between the first decade of the 21st century relative to the 1980s and 1990s [*McPhaden et al.*, 2011].

To better observe how trends in the zonal gradient of the thermocline along the equator have impacted subsurface currents and heat content, the linear trend from 1990 to 2009 in subsurface temperatures and the zonal, meridional, and vertical components of the current velocity (U, V, and W, respectively) were calculated and reported at each grid point (Figures 5b, 6b, and 6d). Stippling and the plotted current vectors represent significance
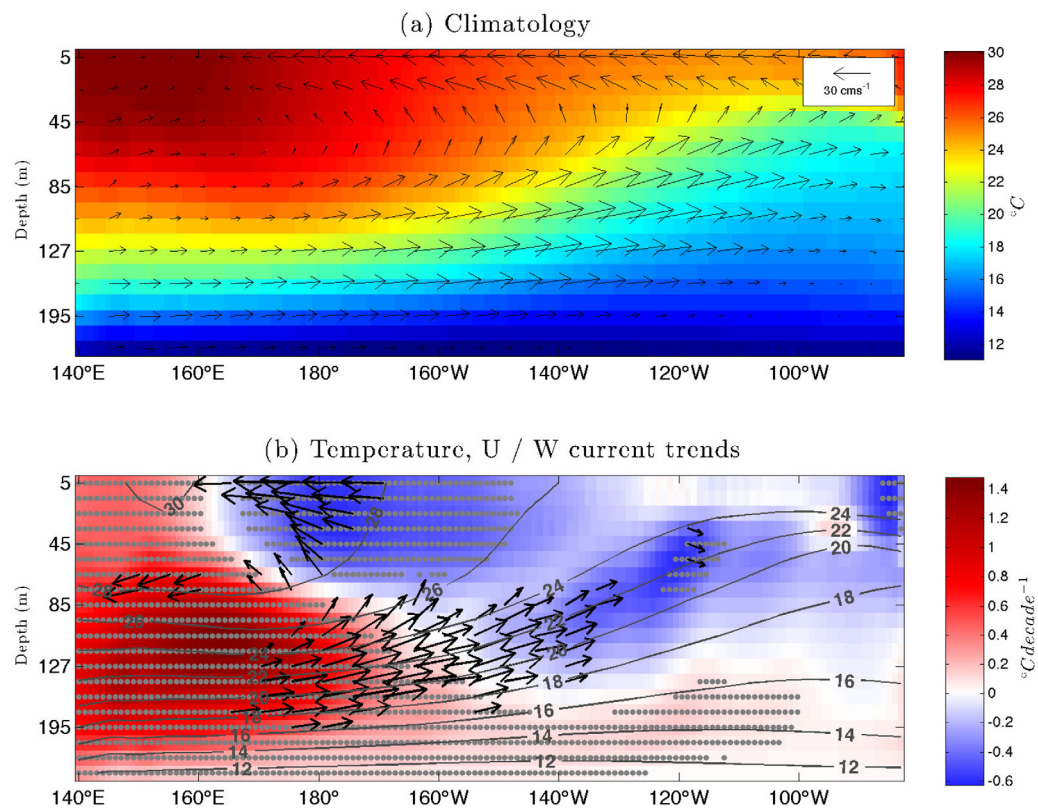
Figure 5. Longitude/depth cross sections of temperature (shading) and currents (vectors) averaged over 2.5°S–2.5°N for (a) mean climatology (1980–2010) and the linear trends during 1990–2009 (b). Temperature trends (°C decade^{-1}) are in shading and U/W current trends (cm s^{-1} decade^{-1}) are black vectors. Gray contours in (b) represent the mean climatology of temperature. Stippling indicates temperature trend significance at the 95% level. Current vectors are only plotted where significant at the 95% level. The maximum current trend vector represents 8.5 cm s^{-1} decade^{-1}. Note: in the figure, the vertical velocity component of current vectors has been scaled by 10^4.
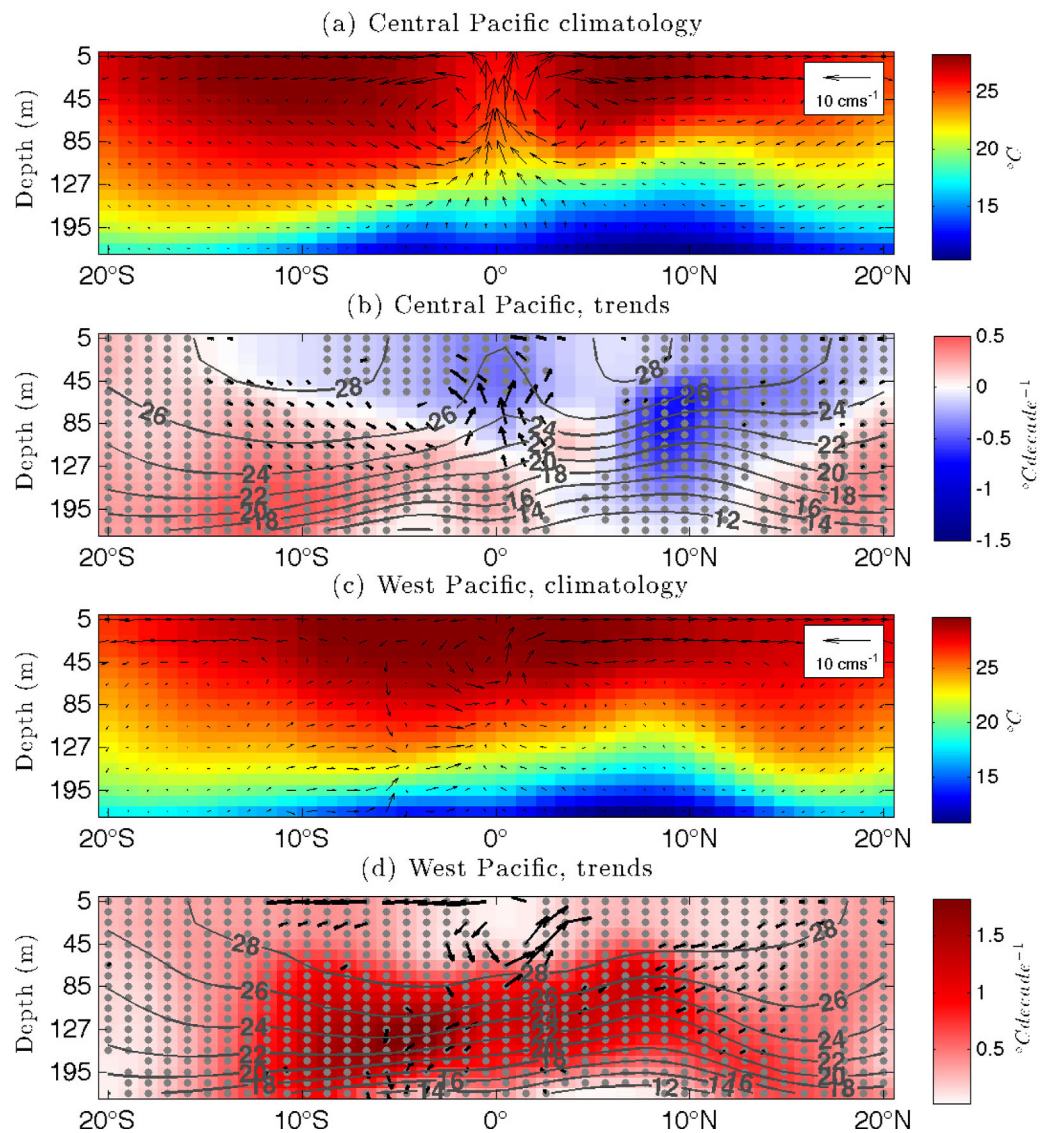
Figure 6. Same as Figure 5, but a latitude/depth cross sections of temperature and currents. Averaged from 180° to 120°W (a, b) and 140°E to 180° (c, d). Gray contours in Figures 6b and 6d represent the mean climatology of temperature for the respective region. Stippling and vectors represent significance at the 95% level. The maximum current trend vector represents 2.5 cm s^{-1} decade^{-1} and 3.2 cm s^{-1} decade^{-1} for Figures 6b and 6d, respectively.

at 95% for the subsurface temperature trends current velocity trends. Climatological cross sections are included in Figures 5a, 6a, and 6c for reference.

Longitude/depth cross sections of the equatorial Pacific are characterized by strong, climatological westward flow from 5 to 20 m, and even stronger return flow eastward in the form of the Equatorial Undercurrent (EUC) at around 125–175 m (Figure 5a). In Figure 5b, there is a pool of warming temperature trends seemingly "trapped" at 75–200 m at 140°E–170°W, while a La Niña-like pattern of decreasing SST trends dominate the cross section from the surface to about 85 m in the central/east regions. The mixed layer cooling in the central Pacific (165°E–150°W) overrides the subsurface warming, and coincides with strong westward surface flow trends. These structures are consistent with intensified westward advection of cold water. Additionally, the subsurface warming in the western Pacific (Figure 5b) is consistent with a similar heat anomaly described by *England et al.* [2014] in a numerical simulation of the ocean driven by observed surface winds.

The cooling trends in the central and eastern equatorial Pacific surface waters are indicative of a shoaling thermocline, while the warming trends in the western subsurface indicates thermocline deepening. This is

consistent with the increasing trend observed in the zonal gradient of the thermocline (Figure 4). Significant strengthening in the zonal slope of the thermocline would lead to anomalous subsurface pressure gradients that accelerate the EUC from about 170°E–140°W over the 20 year period (Figure 5b). The core of the climatological EUC is found around 85–127 m, 150°W–130°W and has an average magnitude of 37 cm s^{-1} in the reanalysis (Figure 5a). The most significant trends in the zonal component of the subsurface currents lie further west and are deeper around 105–155 m, 180°–160°W and have an average magnitude of 6.9 cm s^{-1} decade^{-1} (Figure 5b). GECCO2 underestimates the strength of the observed zonal current in the background state [e.g., *Johnson et al.*, 2002], but the linear trend estimated from GECCO2 is similar to that observed by TAO/TRITON moored buoys for the same period (see Figure 13).

To investigate the cross-equatorial structure, Figure 6 describes latitude/depth cross sections in the central and west Pacific (180°–120°W and 140°E–180°, respectively). In the central Pacific, the average climatological rate of upwelling on the equator is 1.3×10^{-3} cm s^{-1} and occurs between 50 and 85 m, while the most significant upwelling trends occur at the same depths and have an average value of 2.0×10^{-4} cm s^{-1} decade^{-1} (Figures 6a and 6b). This upwelling trend integrated from 170° to 120°W and 0.5°S–0.5°N produces a volume transport trend of 11.1 Sv decade^{-1} from 1990 to 2009, which is in good agreement with the 9 Sv change in vertical transport across the late 1990s transition from a positive to negative PDO reported by *McPhaden and Zhang* [2004]. Increased upwelling could therefore be contributing to the cooling trends observed in the mixed layer and at the surface in Figures 2 and 5b.

In the west Pacific climatological cross section, the currents right on and just south of the equator are dominated by northward flow from 45 to 200 m (Figure 6c). In Figure 6d, these currents are significantly intensified by about 0.92 cm s^{-1} decade^{-1} from 1990 to 2009 just south of and on the equator. There appears to be a stronger southern hemisphere component (5°S–10°S) to the warming subsurface trends observed in Figure 5b. Additionally, these temperature trends seem to roughly line up with the strongest intensifying trends of the subducting branch of the meridional overturning circulations, which can be found at around between 15°S and 5°S in the central Pacific (Figure 6b) and between 4°S and the equator in the western Pacific (Figure 6d). Combined with the increased equatorward flow, this enhanced subduction may imply the presence of enhanced meridional temperature advection seen in previous studies [e.g., *England et al.*, 2014; *Yang et al.*, 2014].

3.2. Seasonality and Observational Comparison

To better understand how the above results vary seasonally, a series of time/longitude plots were generated. Figure 7a shows trends in SST and the zonal wind stress for each calendar month for 1990–2009 averaged over 2.5°S–2.5°N and from 140°E to 80°W. Figures 7b and 7c show trends in SSH and the depth of the 20°C isotherm, respectively (D20); both with the same trend in zonal surface current overlaid and averaged over the same latitude intervals. The convention for D20 trends is such that positive values represent a deepening trend and negative values represent a shoaling trend. The dark gray stippling indicates trend significance at 90%, while light gray represent 80% significance. For the zonal wind stress and zonal surface current trends, the black vectors represent 90% significance and light gray vectors are 80% significance. We limit trends in surface wind stress and surface currents to only the zonal component because it dominates the overall trend in the vector fields (not shown). To the left of each time/longitude section, the corresponding seasonal cycle of the wind stress/current trends averaged from 160°E to 150°W is plotted in blue, while the mean 1990–2009 means seasonal cycle in the same box for the respective variable is in green.

In Figure 7a, the decreasing trend observed in Figure 2 is most pronounced from December to May (DJFMAM) while weak cooling or warming trends are found from June to November (JJASON). This result is consistent with studies by *Kosaka and Xie* [2013] and *Trenberth et al.* [2014]. There is evidence that the SST trends are responding to an enhancement of the mean seasonal cycle of the zonal wind stress as indicated by the significant easterly wind stress trends (blue line) during NDJFMA, which is typically a time of relatively strong climatological easterly flow (green line). Additionally, the easterly wind stress trends are weakest in MJJASO when the mean trades are also at their weakest (Figure 7a, side plot). The relationship described above for wind stress trends holds most consistently for the central Pacific, while the trend in the seasonal SST cycle holds from 160°E to 90°W.

Surface currents near the equator are primarily driven by the wind stress, as the Coriolis force is very small. An enhancement of the seasonal cycle of the wind stress should therefore correspond to an enhancement
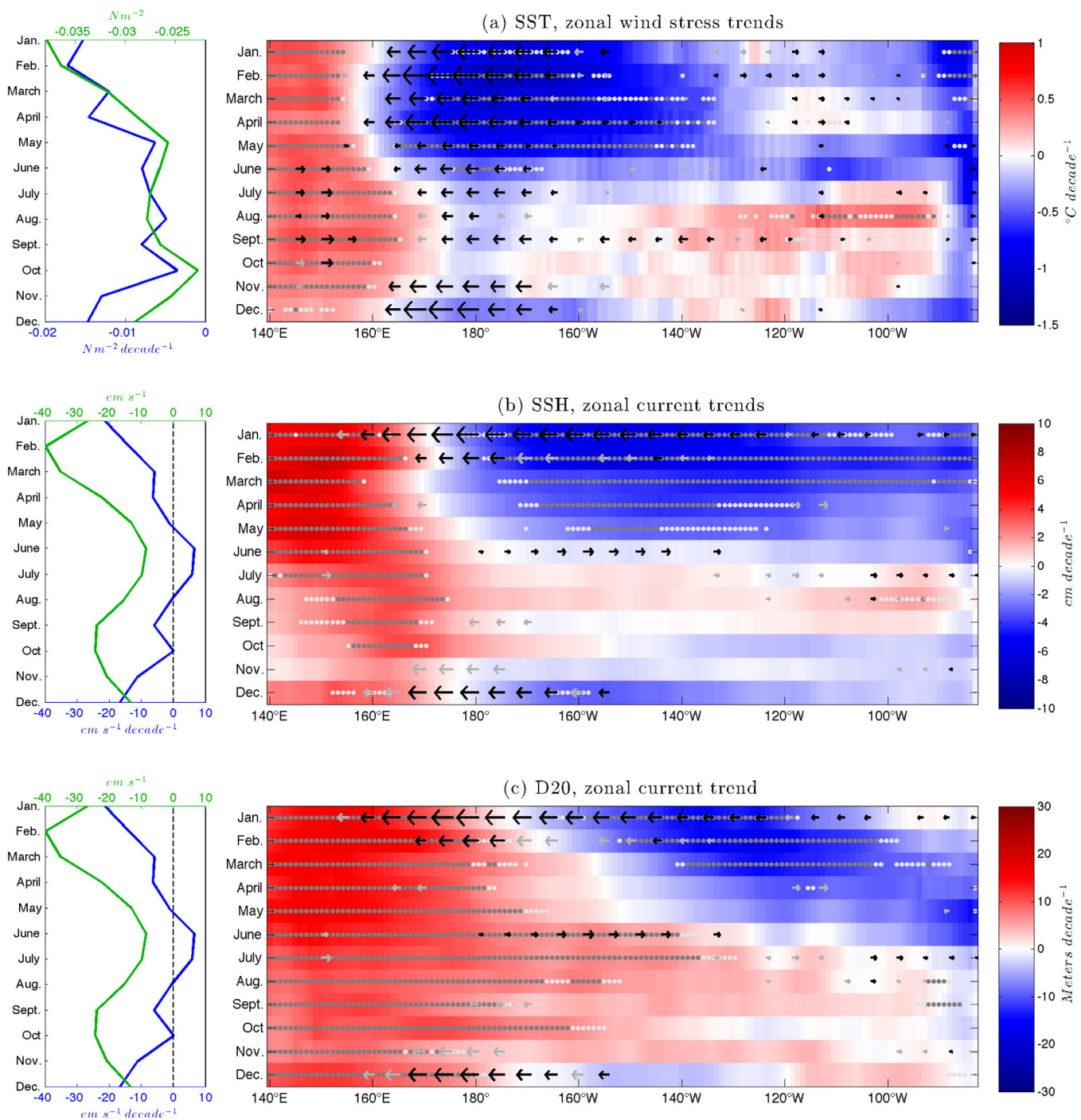
Figure 7. Time/longitude plots of the 1990–2009 trends in SST (a, °C decade^{-1}), SSH (b, cm decade^{-1}), and D20 (c, m decade^{-1}) in shading and zonal wind stress (a only, N m^{-2} decade^{-1}) or 5 m zonal current (b and c, cm s^{-1} decade^{-1}) averaged from 2.5°S to 2.5°N. Zonal wind stress trends in Figure 7a and zonal current velocity trends in Figures 7b and 7c averaged from 160°E to 150°W are shown in corresponding seasonal cycles to the left in blue. The mean 1990–2009 seasonal cycles for zonal wind stress (N m^{-2}) and zonal current velocity (cm s^{-1}) are in green. Dark gray and light gray stippling represents temperature trends significant at 90% and 80%, respectively. Zonal wind stress and zonal current velocities are black for 90% significance and light gray for 80%. The maximum zonal wind stress trend vector represents 0.03N m^{-2} decade^{-1} and the maximum current trend vector represents 26 cm s^{-1} decade^{-1}.

in the seasonal cycle of surface currents and zonal temperature advection (Figures 7b, 7c, and 8). Trends in SSH reflect the weakening and strengthening of the zonal wind stress as water is piled up in the west during DJFMAM and is allowed to slosh back during JJASON (Figure 7b). The surface currents also respond to the waxing and waning of the wind stress. Strong westward/eastward trends in equatorial flow from 160°E
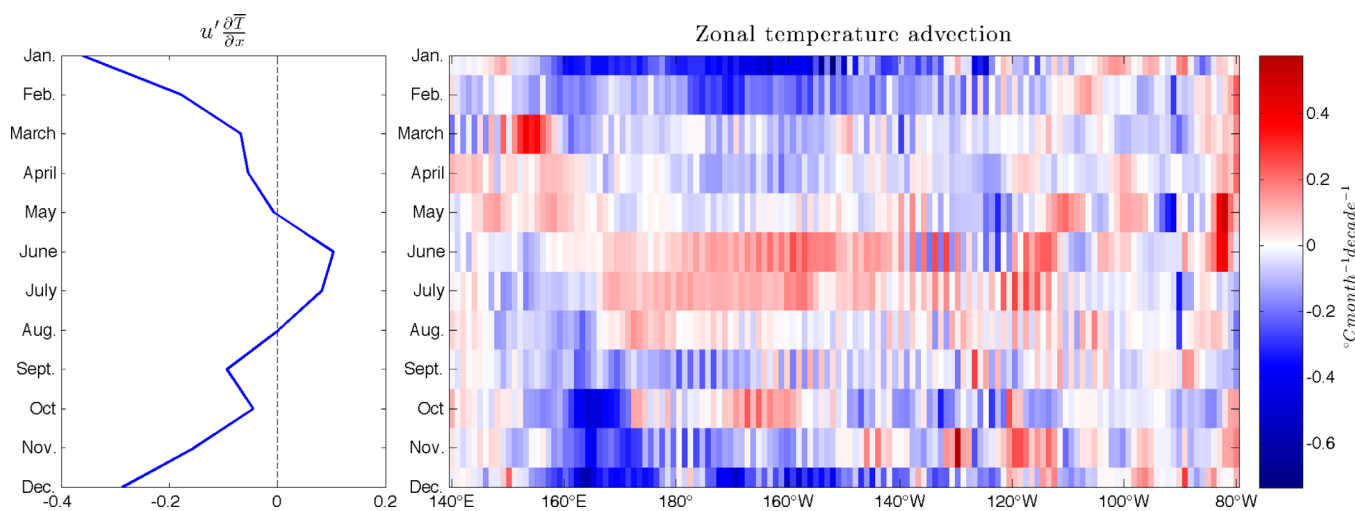
Figure 8. Same as Figure 7, but zonal surface temperature advection trends (°C month^{-1} decade^{-1}) from 1990 to 2009. Zonal temperature advection trends averaged from 160°E to 150°W are shown to the left. This data were taken from the raw model grid.

to about 120°W are dominant during times of strong/weak easterly wind stress. Additionally, trends in SST persist for about 3 months after the most significant trends in surface currents. The westward equatorial flow trends in NDJF would tend to build SSH in the west Pacific and decrease SSH in the central/east Pacific. We observe this as positive SSH trends from 140°E to 160°E and negative SSH trends from 180° to 80°W in DJFMAM (Figure 7b). Additionally, the westward flow would advect climatologically cold-water westward and increase subsurface upwelling in the central Pacific, setting up the SST trends observed in DJFMAM (Figures 7a, 6b, and 8). As the westward flow trend weakens and disappears in February, the cold SST and low SSH trends persist for 3 months before responding to an eastward surface current trend in June–July.

During these months, the climatological surface flow is westward at an average rate of 9.15 cm s^{-1}, while the trend in the zonal current is eastward at 6.13 cm s^{-1} decade^{-1} (Figures 7b and 7c side plots). The eastward trend would tend to significantly slow down the mean equatorial flow, reducing the build up of water in the western basin as well as decreasing the removal of water in the east. Consequently, SSH increases in the central/east Pacific and decreases in the west Pacific over the 20 year period (Figure 7b). In addition, the eastward surface current trends would generate a tendency toward warm-water advection in the west Pacific eastward, increasing SST in JJASON (Figures 7a and 8). Similarly, the positive SST and SSH trends persist 3–4 months after the eastward flow weakens in July. The abrupt reversal in surface current trends is surprising and may be explained by the fact that the zonal wind stress trends always have relatively strong easterly component from 170°E to about 120°W during the 20 year period (Figures 1b and 7a). A west-to-east reversal in the surface current trends is therefore likely due to the weakening of the easterly wind stress from April to August. Ultimately, the trends in the zonal surface current are acting to enhance the mean seasonal cycle seen in Figures 7b and 7c (left).

Although the boreal summer and fall trends in SST and SSH are insignificant, they do elicit a significant trend of D20 (Figure 7c). In December, trends of D20 are largely negative from about 170°W–120°W. Over the following 5 months, the shoaling D20 trends steadily shift eastward, and as a result, the increasing trend in the zonal gradient of D20 is most pronounced in boreal winter and spring (Figures 4 and 7c). The opposite case occurs in May when positive (deepening) D20 trends are located throughout the entire west and central Pacific from 140°E to 160°W. The deepening thermocline then propagates eastward from June to November, flattening the trend in the zonal gradient of D20.

A full heat budget analysis was not possible using the GECCO2 data set as the required budget terms were not saved. Instead, we provide a qualitative illustration of the trend in zonal advection of temperature anomalies from 2.5°S to 2.5°N during 1990–2009. Figure 8 shows the trends in zonal temperature advection in °C month^{-1} decade^{-1} estimated by finite differencing of monthly means and linear regression. The trend significance in the two components of zonal temperature advection was previously reported in Figures 7. Thus, we leave off stippling in Figure 8 for clarity, as the plot is rather noisy. In particular, the temperature
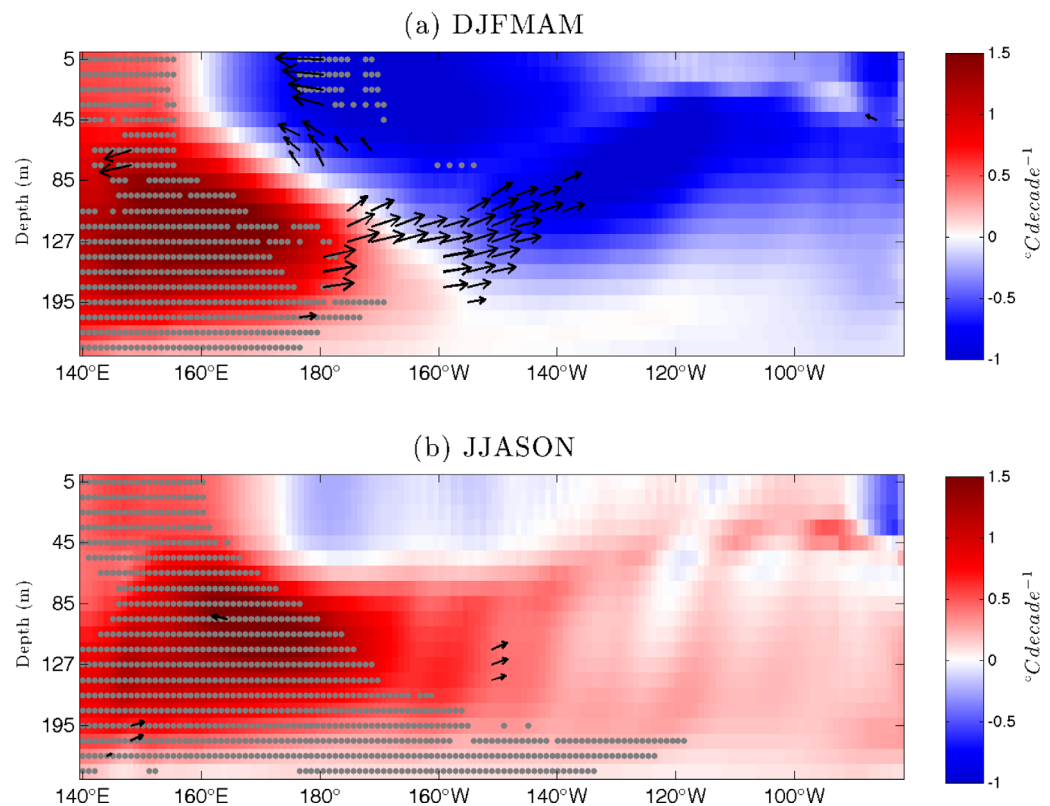
Figure 9. Same as Figure 5b, but linear trends of DJFMAM (a) and JJASON (b) from 1990 to 2009. The maximum current trend vector represents 16.1 cm s^{-1} decade^{-1} and 5.3 cm s^{-1} decade^{-1} for Figures 9a and 9b, respectively.

gradient east of about 130°W is too noisy to produce a confident interpretation; therefore, we limit our analysis to west of this longitude. In NDJF, there is a trend towards enhanced westward cold-water advection on the order of −0.2 to −0.3°C month^{-1} decade^{-1} from about 160°E–150°W, which is consistent with the negative SST trends observed in the following 3 months (Figures 7a and 8). During times of increasingly eastward flow (June–July), there is a trend toward eastward warm-water advection on the order of 0.11°C month^{-1} decade^{-1}. The weakening of the climatologic surface flow seen in Figures 7b and 7c would reduce cold-water advection during boreal summer and produce a tendency toward warm-water advection, which is consistent with the positive SST trends seen in Figure 7a for the following 2–3 months.

Trends of D20 have significant impacts on subsurface circulation intensity from 1990 to 2009 (Figures 4 and 5). Therefore, we should expect seasonal variations in trends of D20 to have significant impacts on the seasonal cycle of these subsurface circulations, particularly in the zonal direction (Figure 7c). Figure 9 shows a longitude/depth cross section for the trend in DJFMAM and JJASON from 1990 to 2009. As in Figure 5b, stippling and vectors represent significance at 95% for a Mann-Kendall test. During DJFMAM, there is a strong westward trend in the flow near the surface centered on the dateline, which is consistent with the wind-driven westward equatorial surface flow seen in Figures 7b and 7c. Westward trends in the surface layer are also consistent with the westward advection of cold-water seen in Figure 8 and cooling SST trends in the central/east Pacific (Figure 9a). The subsurface warming trends, first seen in Figure 5b, persist throughout the year, which is consistent with the positive D20 trends shown in Figure 7c. East of 170°W, however, the subsurface temperature trends follow the seasonal variation of the D20 trends with cooling in DJFMAM when the thermocline shoals and warming in JJASON when the thermocline deepens.

The dominant trend in currents below 50 m is a pronounced strengthening of the EUC from 180° to 140°W on the order of 9 cm s^{-1} decade^{-1}. This is generally consistent with a stronger zonal gradient in D20 during this time of the year (Figures 4 and 7c). Overall, Figure 9a depicts an intensifying zonal wind-driven circulation. In contrast, during JJASON the D20 zonal gradient trend, while not zero, is substantially weaker and not significant compared to the DJFMAM trend (Figure 7c). Recall from Figure 5b, the most significant
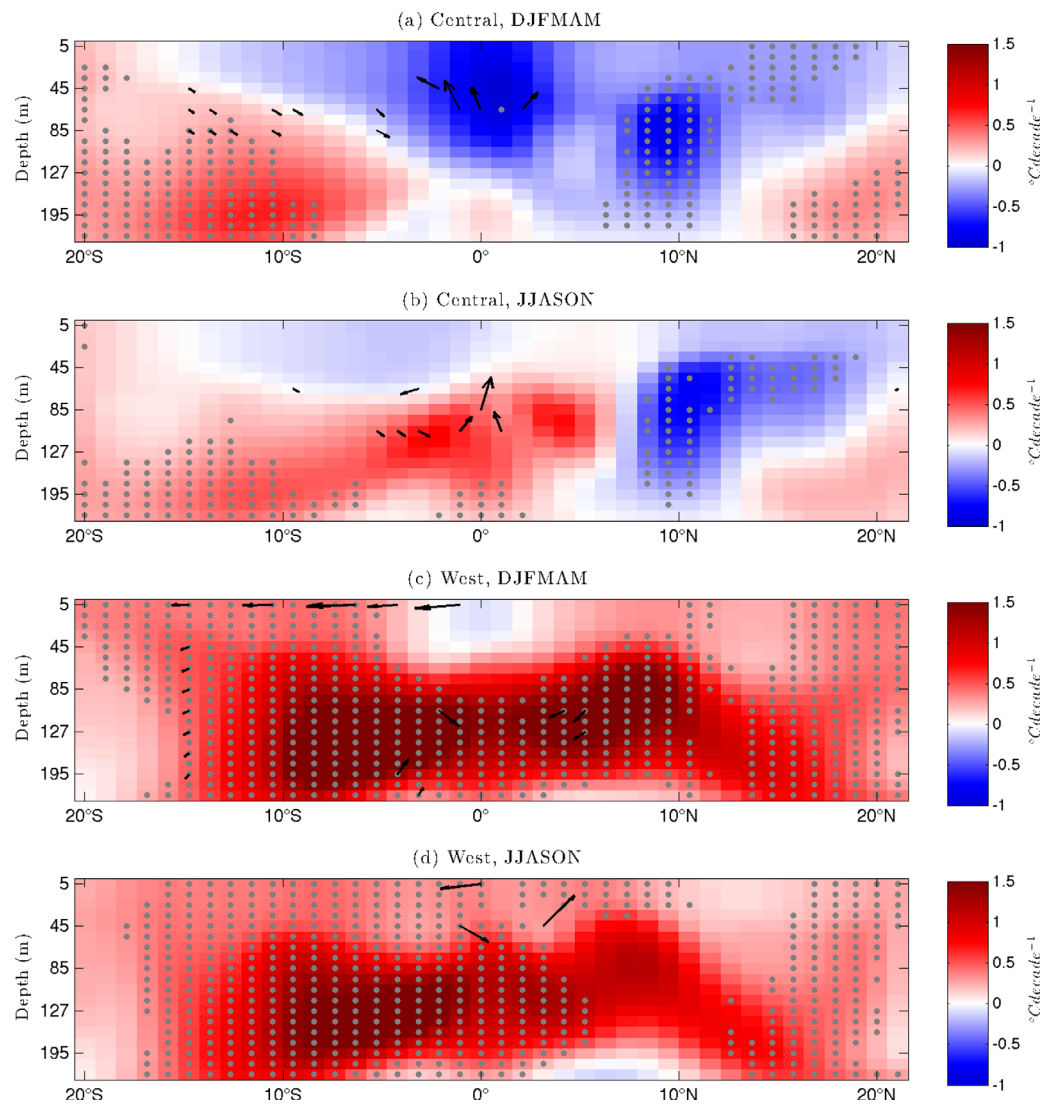
Figure 10. Same as Figures 6b and 6d, but averaged over DJFMAM (a) and JJASON (b). The maximum current trend vector represents 2.96, 3.2, 2.8, and 3.5 cm s^{-1} decade^{-1} for Figures 10a–10d, respectively.

annual mean trend of the EUC is 6.9 cm s^{-1} decade^{-1}. The trend in the EUC during DJFMAM is greater than the annual mean trend while the JJASON trend is much less (4 cm s^{-1} decade^{-1}), indicating that the most significant increase in the strength of the EUC occurs in the boreal winter and spring.

Figure 10 is the same as Figure 9 except for meridional cross sections of the central and west Pacific. During DJFMAM, the central Pacific is experiencing strong cooling from the surface to about 100 m on the equator and around 10°N (Figure 10a). On the equator and near 2°S, there are significant current trends showing increased upwelling that could be contributing to the equatorial cooling. During JJASON, however, the strong cooling in the central equatorial Pacific gives way to warming trends along the equator while the cooling trends persist around 10°N. These equatorial variations occur in spite of stronger trends in upwelling during JJASON compared to DJFMAM. This suggests that seasonal variations in central equatorial Pacific temperature trends are dominated by seasonal variations in the trends of D20 and zonal temperature advection, which show a similar seasonal cycle (Figures 7c, 8, 10a, and 10b).

In the west Pacific, significant warming trends occur throughout much of the subsurface during DJFMAM and JJASON, with a slight southern hemisphere asymmetry. The persistent warming trends could be due to the consistent deepening trends observed in D20 (Figure 7c); however, it is possible that the intensified subduction and equatorward flow seen in the annual mean trend is increasing meridional advection of
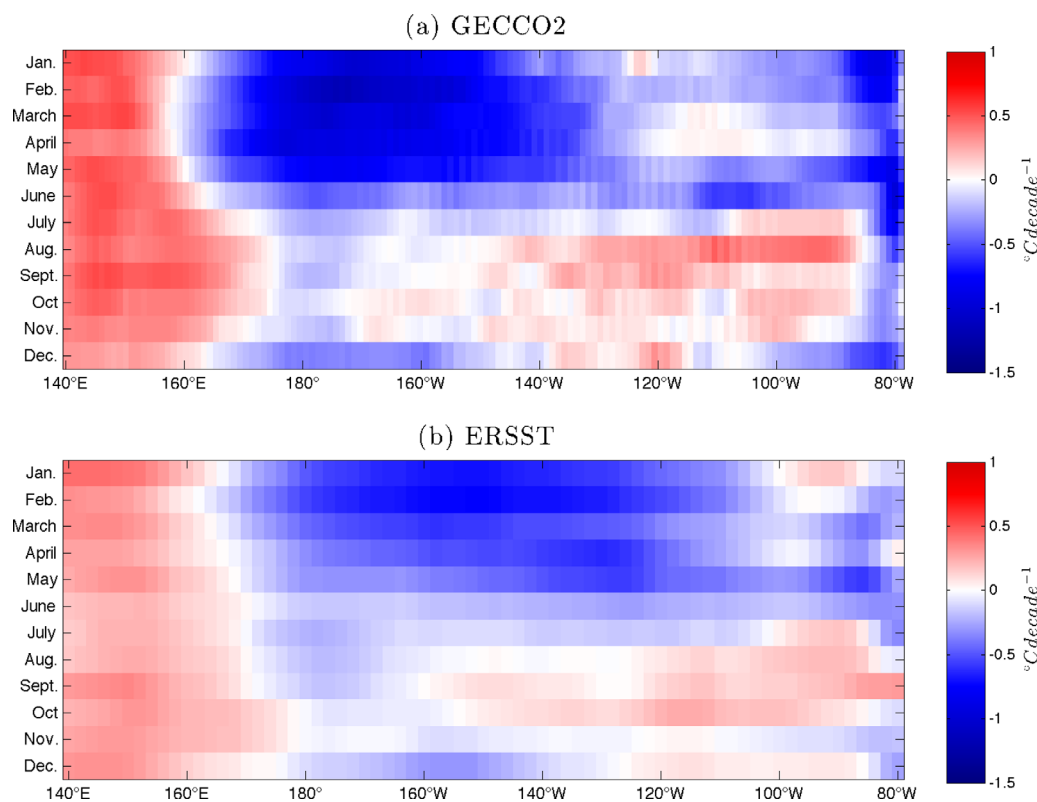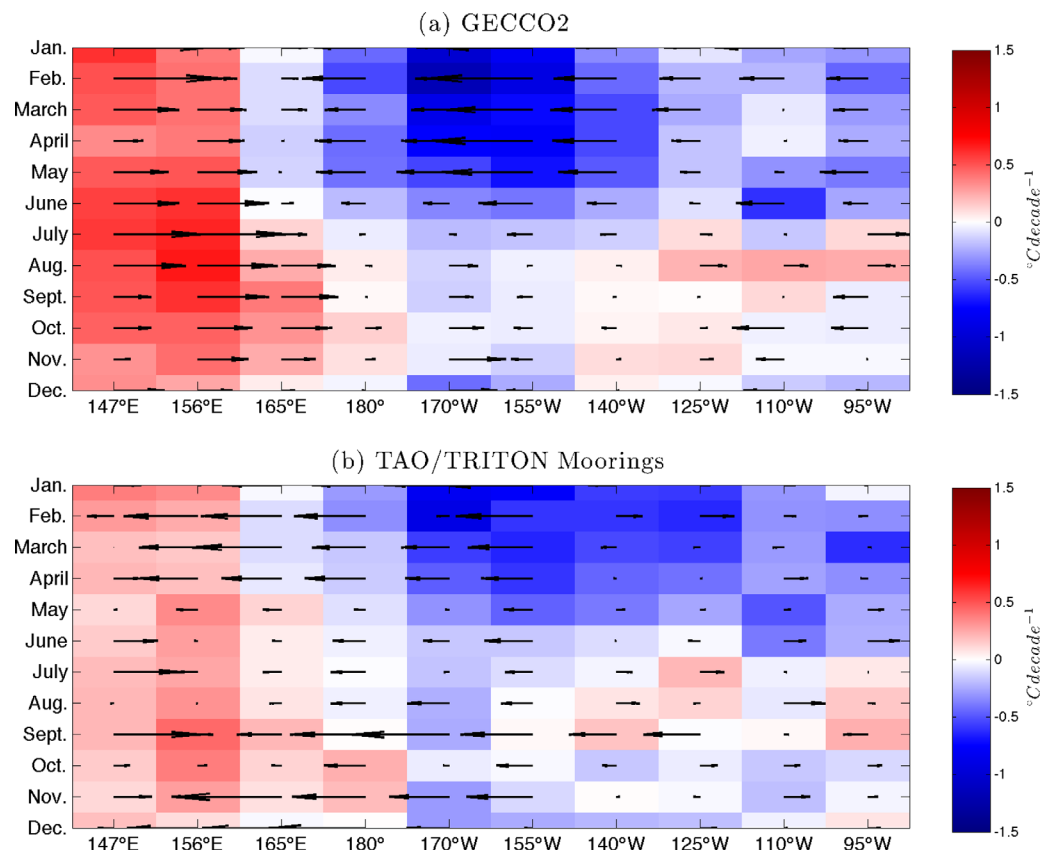
Figure 11. Same as Figure 7a, but for GECCO2 (a) and ERSST-averaged SST (b) trends.

warm water from 1990 to 2009 and significantly contributing to the subsurface warming trends (Figures 6d, 10c, and 10d).

All of the above GECCO2 SST results were compared with ERSST data and were generally consistent. For brevity, we include only the time-latitude average of SST trends in the equatorial Pacific (Figures 11). Like GECCO2, the observations also support a seasonal variation in the SST trend with cooling most prominent in DJFMAM and diminishing to neutral or warming conditions in JJASON. It should be noted that the magnitude of GECCO2 SST trends is slightly higher for a given trend relative to ERSST.

Similarities between GECCO2 and TAO/TRITON SST trends are to be expected because TAO/TRITON vertical temperature profiles were among the data assimilated into GECCO2 [*Köhl and Stammer*, 2008]. Nevertheless, a 30 year 4D-var assimilation may not necessarily reproduce observed SST accurately. Thus, time-latitude averages of SST and zonal wind stress trends measured by the TAO/TRITON array were generated and compared to GECCO2 (Figure 12). There exist large data gaps in the TAO/TRITON SST and zonal wind stress products due to instrument failure, particularly in the west/central Pacific. Therefore, it was necessary to resample GECCO2 data to be temporally and spatially consistent with TAO/TRITON data. When comparing Figures 12a and 12b, there is a strong spatial correlation in the magnitude and timing of SST trends between the resampled GECCO2 data and TAO/TRITON. Moorings east of 170°W demonstrate a strong seasonality in the 20 year cooling trends that is consistent with both ERSST and GECCO2. Moorings west of 170°W do not show such a striking seasonal dependence, which is also consistent with the notion that the majority of the seasonal cycle observed in GECCO2 was found in the central/east Pacific. The trend in the zonal wind stress is also generally consistent in the central Pacific with the most easterly trends occurring in boreal winter and the weakest in the summer.

Figure 13b shows the trend in ADCP-measured zonal current velocity taken by equatorial TAO/TRITON moorings. There is an eastward trend to the EUC at 165°E, 170°W, 140°W, and 110°W with the strongest component ranging from 11 cm s^{-1} decade^{-1} at about 200 m to 16 cm s^{-1} decade^{-1} about 100 m from

Figure 12. Same as Figure 7a, but for GECCO2 SST and zonal wind stress trends (a) and TAO/TRITON SST and zonal wind stress trends (b). All moorings from 5°S to 5°N were averaged along each longitude line. The maximum zonal wind stress vector represents 0.91 N m^{-2} decade^{-1} and 0.02 N m^{-2} decade^{-1} for Figures 12a and 12b, respectively.

west to east. Figure 13a shows the trend in GECCO2-derived zonal currents, resampled to be spatially consistent with the available TAO/TRITON ADCP data. GECCO2 shows a positive trend in the EUC from 1990 to 2009 at 165°E, 170°W, and 140°W, but it fails to reproduce the anomalous eastward flow at 110°W (Figure 13b). Additionally, GECCO2 tends to underestimate the observed trend in the zonal current velocity with maximum values of about 5 cm s^{-1} decade^{-1} and 10 cm s^{-1} decade^{-1}, west-to-east. This depth difference, however, is consistent with the shoaling of the EUC from west to east in tandem with the thermocline. In general, GECCO2 consistently captures the observed structure of current variability, but has a weaker trend than observed during the transition to the hiatus period.

4. Summary and Discussion

The response of equatorial Pacific surface and subsurface dynamics to a consistent increase in zonal wind stress during the transition from a non-hiatus (positive PDO) to the present hiatus period (negative PDO) was quantified using an ocean reanalysis product. Comparisons to observational data from ERSST and TAO/TRITON moorings were generally consistent with GECCO2 results. It was found that surface waters have been anomalously advected further westward over the past 20 years along the equatorial Pacific. Associated changes to SSH and zonal thermocline depth gradients were associated with a more vigorous wind-driven subsurface circulation consistent with previous studies using models that were not constrained with observations [e.g., *England et al.*, 2014].

The trends discussed in this study bear resemblance to longer centennial time-scale trends reported elsewhere. For example, *Drenkard and Karnauskas* [2014] show a 20th century deepening and westward shift of the EUC core that is similar to Figure 5b using a different reanalysis product. *Yang et al.* [2014] also show a long-term strengthening over 1900–2008 of tropical Pacific interior flow associated with a spin up of Pacific
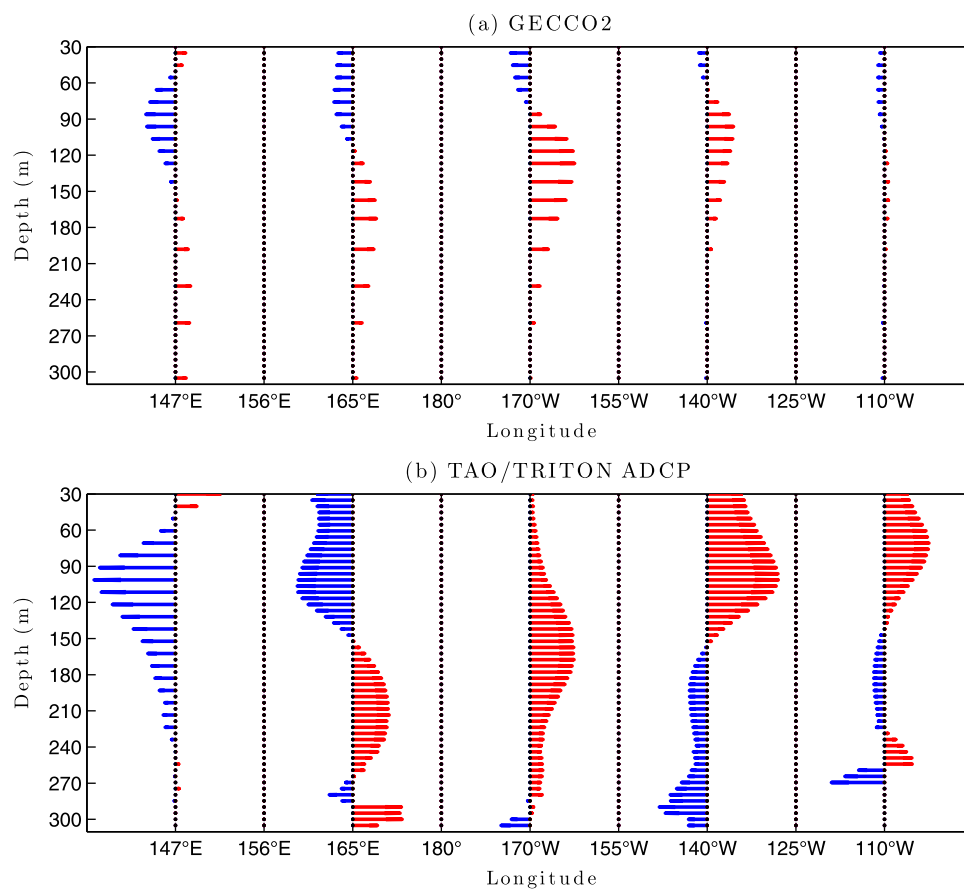
Figure 13. TAO/TRITON mooring ADCP measurements of the zonal current velocity trend at 0° latitude (a) and GECCO2-derived zonal current velocity trends at 0.5° latitude (b). Red vectors represent eastward trends (cm s^{-1} decade^{-1}), while blue represents westward trends. The maximum current trend vector represents 16.0 cm s^{-1} decade^{-1} and 10.1 cm s^{-1} decade^{-1} for Figures 13a and 13b, respectively.

subtropical cells that is comparable to Figure 6. Nevertheless, the trends reported here are larger than the longer time scale trends, most likely because they are due to more energetic processes operating on shorter decadal time scales associated with, for example, the PDO. Some of the physical processes involved in these two time scales may be similar, though an analysis to determine the degree of correspondence is beyond the scope of this study. Additional investigation is also needed to clarify whether the trends we described are associated with changes in ENSO statistics [*McPhaden et al.*, 2011]. For example, the SST trends in Figure 2 are reminiscent of a central Pacific La Niña pattern [e.g., *Ashok et al.*, 2007; *Lee and McPhaden*, 2010], which has been the focus of major research efforts in recent years [e.g., *Capotondi et al.*, 2015; *Amaya and Foltz*, 2014].

A major finding of this study is that the seasonal variations during this transitional period are driven by seasonal variations in zonal advection trends of climatologic surface waters and the seasonal deepening/shoaling of the thermocline that influence equatorial upwelling. These surprising reversals in current trends and enhanced/weakened upwelling combine to cause anomalous cooling in DJFMAM and anomalous warming in JJASON. Changes in the surface currents appear to be driven by variations in the strength of the easterly wind stress. A further consequence of the seasonal reversal of the anomalous surface current is a seasonal variation in the strength of zonal and meridional wind-driven subsurface circulations along the equator. The seasonal spinning up and slowing down of these subsurface circulations has important impacts on the redistribution of heat in the tropical Pacific Ocean. A quantitative analysis using a model with a consistent and complete heat budget is needed to evaluate this further and should be the focus of future studies.

During the recent hiatus, the global mean SAT trend showed a pronounced seasonality, positive during the boreal winter and negative during summer [*Cohen et al.*, 2012]. In the limit that the tropical Pacific is the

driving force behind the hiatus, *Kosaka and Xie* [2013] suggested that seasonal differences in Northern Hemisphere teleconnections induced by tropical Pacific SST anomalies cause the seasonality of global mean SAT trend. Our results differ from their work in that we show a pronounced seasonal variation in the La Niña-like pattern in the tropics, which may cause a seasonal variation in tropical atmospheric cooling. The seasonality of decadal variability has not been rigorously investigated. The results of these two studies motivate further research into decadal seasonal variations and how such variability impacts remote climates and projects onto global SAT trends.

Pinpointing the missing heat associated with the global warming hiatus is crucial to our understanding of such events [e.g., *Balmaseda et al.*, 2013; *Chen and Tung*, 2014; *Kintisch*, 2014; *England et al.*, 2014]. While uncertainties regarding the magnitude [*Karl et al.*, 2015] and the mechanisms driving the beginning and end of a hiatus remain, its impact on climatically significant regions such as the tropical Pacific can be identified. This study takes an important step toward increasing our understanding of the region and may help to improve our ability to predict both regional and remote climate variability associated with transitions into future hiatuses. Hiatus periods are likely to affect future decadal warming trends [*Easterling and Wehner*, 2009; *Hansen et al.*, 2011], so continuing to improve our understanding of their causes and consequences and should be a high priority for additional research.

References

Amaya, D. J., and G. R. Foltz (2014), Impacts of canonical and Modoki El Nino on tropical Atlantic SST, *J. Geophys. Res. Oceans*, *119*, 777–789, doi:10.1002/2013JC009476.

Ashok, K. et al. (2007), El Niño Modoki and its possible teleconnection, *J. Geophys. Res.*, *112*, C11007, doi:10.1029/2006JC003798.

Balmaseda, M. A., K. E. Trenberth, and E. Källén (2013), Distinctive climate signals in reanalysis of global ocean heat content, *Geophy. Res. Lett.*, *40*, 1754–1759, doi:10.1002/grl.50382.

Brown, P., W. Li, and S.-P. Xie (2015), Regions of significant influence on unforced global mean surface air temperature variability in climate models, *J. Geophys. Res. Atmos.*, *120*, 480–494, doi:10.1002/2014JD022576.

Capotondi, A. et al. (2015), Understanding ENSO diversity, *Bull. Am. Meteorol. Soc.*, *96*, 921–938, doi:10.1175/BAMS-D-13-00117.1.

Chen, X., and K. K. Tung (2014), Varying planetary heat sink led to global-warming slowdown and acceleration, *Science*, *354*(6199), 897–903, doi:10.1126/science.1254937.

Cohen, J. L., J. C. Furtado, M. Barlow, V. A. Alexeev, and J. E. Cherry (2012), Asymmetric seasonal temperature trends, *Geophys. Res. Lett.*, *39*, L04705, doi:10.1029/2011GL050582.

Dai, A., J. C. Fyfe, S.-P. Xie, and X. Dai (2015), Decadal modulation of global surface temperature by internal climate variability, *Nat. Clim. Change*, *5*, 555–559, doi:10.1038/nclimate2605.

Drenkard, E. J., and K. B. Karnauskas (2014), Strengthening of the Pacific equatorial undercurrent in the SODA reanalysis: Mechanisms, ocean dynamics, and implications, *J. Clim.*, *27*, 2405–2416, doi:http://dx.doi.org/10.1175/JCLI-D-13-00359.1.

Easterling, D. R., and M. F. Wehner (2009), Is the climate warming or cooling?, *Geophys. Res. Lett.*, *36*, L08706, doi:10.1029/2009GL037810.

England, M. H., S. McGregor, P. Spence, G. A. Meehl, A. Timmermann, W. Cai, A. S. Gupta, and M. J. McPhaden (2014), Recent intensification of wind-driven circulation in the Pacific and the ongoing warming hiatus, *Nat. Clim. Change*, *4*, 222–227, doi:10.1038/nclimate2106.

Folland, C. K., T. R. Karl, and M. Jim Salinger (2002), Observed climate variability and change, *Weather*, *57*, 269–278, doi:10.1256/004316502320517353.

Guemas, V., F. J. Doblas-Reyes, I. Andreu-Burillo, and A. Muhammad (2013), Retrospective prediction of the global warming slowdown in the past decade, *Nat. Clim. Change*, *3*, 649–653, doi:10.1038/nclimate1863.

Hansen, J., M. Sato, R. Ruedy, K. Lo, D. W. Lea, and M. Medina-Elizade (2006), Global temperature change, *Proc. Natl. Acad. Sci. U. S. A.*, *103*(39), 14,288–14,293, doi:10.1073/pnas.0606291103.

Hansen, J., R. Ruedy, M. Sato, and K. Lo (2010), Global surface temperature change, *Rev. Geophys.*, *48*, RG4004, doi:10.1029/2010RG000345.

Hansen, J., M. Sato, P. Kharecha, and K. von Schuckmann (2011), Earth's energy imbalance and implications, *Atmos. Chem. Phys.*, *11*, 13,421−13,449, doi:10.5194/acp-11-13421-2011.

Hartmann, D. L., et al. (2013), Observations: Atmosphere and surface, In *Climate Change 2013: The Physical Science Basis. Contribution of Working Group I to the Fifth Assessment Report of the Intergovernmental Panel on Climate Change*, edited by T. F. Stocker et al., Cambridge Univ. Press, Cambridge, U. K.

Johnson, G. C., B. M. Sloyan, W. S. Kessler, and K. E. McTaggart (2002), Direct measurements of upper ocean currents and water properties across the tropical Pacific during the 1990s, *Prog. Oceanogr.*, *52*(1), 31–36, doi:10.1016/S0079-6611(02)00021-6.

Karl, T. R., A. Arguez, B. Huang, J. H. Lawrimore, J. R. McMahon, M. J. Menne, T. C. Peterson, R. S. Vose, and H.-M. Zhang (2015), Possible artifacts of data biases in the recent global surface warming hiatus, *Science*, *348*(6242), 1469–1472, doi:10.1126/science.aaa5632.

Katsman, C. A., and G. J. van Oldenborgh (2011), Tracing the upper ocean's "missing heat," *Geophys. Res. Lett.*, *38*, L14610, doi:10.1029/2011GL048417.

Kaufmann, R. K., H. Kauppi, M. L. Mann, and J. H. Stock (2011), Reconciling anthropogenic climate change with observed temperature 1998-2008, *Proc. Natl. Acad. Sci. U. S. A.*, *108*(29), 11,790–11,793, doi:10.1073/pnas.1102467108.

Keenlyside, N. S., M. Latif, J. Jungclaus, L. Kornblueh, and E. Roeckner (2008), Advancing decadal-scale climate prediction in the North Atlantic sector, *Nature*, *453*, 84–88, doi:10.1038/nature06921.

Kendall, M. G. (1975), *Rank Correlation Methods*, 202 pp., Charles Griffin, Oxford Univ. Press, London, U. K.

Kintisch, E. (2014), Is Atlantic holding Earth's missing heat?, *Science*, *345*(6199), 860–861, doi:10.1126/science.345.6199.860.

Kosaka, Y., and S.-P. Xie (2013), Recent global-warming hiatus tied to equatorial Pacific surface cooling, *Nature*, *501*, 403–407, doi:10.1038/nature12534.

Köhl, A. (2014), Evaluation of the GECCO2 ocean synthesis: Transports of volume, heat and freshwater in the Atlantic, *Q. J. R. Meteorol. Soc.*, *141*, 166–181, doi:10.1002/qj.2347.

Köhl, A., and D. Stammer (2008), Variability of the Meridional overturning in the North Atlantic from the 50-Year GECCO state estimation, *J. Phys. Oceanogr.*, *38*, 1913–1930, doi:10.1175/2008JPO3775.1.

Lee, T., and M. J. McPhaden (2010), Increasing intensity of El Niño in the central-equatorial Pacific, *Geophys. Res. Lett.*, *37*, L14603, doi:10.1029/2010GL044007.

Marotzke, J. and P. M. Forster (2015), Forcing, feedback and internal variability in global temperature trends, *Nature*, *517*, 565–570, doi:10.1038/nature14117.

Mantua, N. J., S. R. Hare, Y. Zhang, J. M. Wallace, and R. C. Francis (1997), A Pacific interdecadal climate oscillation with impacts on salmon production, *Bull. Amer. Meteorol. Soc.*, *78*, 1069–1079.

Marshall, J., C. Hill, L. Perelman, and A. Adcroft (1997), Hydrostatic, quasi-hydrostatic, and nonhydrostatic ocean modeling, *J. Geophy. Res.*, *102*(C3), 5733–5752, doi:10.1029/96JC02776.

McGregor, S., A. Timmerman, M. F. Stuecker, M. H. England, M. Merrifield, F. F. Jin, and Y. Chikamoto (2014), Recent Walker circulation strengthening and Pacific cooling amplified by Atlantic warming, *Nat. Clim. Change*, *4*, 888–892, doi:10.1038/nclimate2330.

McPhaden, M. J., and D. Zhang (2004), Pacific Ocean circulation rebounds, *Geophys. Res. Lett.*, *31*, L18301, doi:10.1029/2004GL020727.

McPhaden, M. J., et al. (1998), The Tropical Ocean-Global Atmosphere (TOGA) observing system: A decade of progress, *J. Geophys. Res.*, *103*(C7), 14,169–14,240, doi:10.1029/97JC02906.

McPhaden, M. J., T. Lee, and D. McClurg (2011), El Niño and its relationship to changing background conditions in the tropical Pacific, *Geophys. Res. Lett.*, *38*, L15709, doi:10.1029/2011GL048275.

Meehl, G. A., J. M. Arblaster, J. T. Fasullo, A. Hu, and K. E. Trenberth (2011), Model-based evidence of deep-ocean heat uptake during surface-temperature hiatus periods, *Nat. Clim. Change*, *1*, 360–364, doi:10.1038/nclimate1229.

Meehl, G. A., A. Hu, J. M. Arblaster, J. Fasullo, and K. E. Trenberth (2013), Externally forced and internally generated decadal climate variability associated with the interdecadal Pacific oscillation, *J. Clim.*, *26*, 7298–7310, doi:10.1175/JCLI-D-12-00548.1.

Merrifield M. A., P. R. Thompson, M. Lander (2012), Multidecaal sea level anomalies and trends in the western tropical Pacific, *Geophys. Res. Lett.*, *39*, L13602, doi:10.1029/2012GL052032.

Pohlmann, H., J. H. Jungclaus, A. Köhl, D. Stammer, and J. Marotzke (2009), Initializing decadal climate predictions with the GECCO oceanic synthesis: Effects on the North Atlantic, *J. Clim.*, *22*, 3926–3938, doi:10.1175/2009JCLI2535.1.

Power, S., T. Casey, C. Folland, A. Colman, and V. Mehta (1999), Inter-decadal modulation of the impact of ENSO on Australia, *Clim. Dyn.*, *15*(5), 319–324, doi:10.1007/s003820050284.

Smith, D. M., S. Cusack, A. W. Colman, C. K. Folland, G. R. Harris, and J. M. Murphy (2007), Improved surface temperature prediction for the coming decade from a global climate model, *Science*, *317*(5839), 796–799, doi:10.1126/science.1139540.

Smith, T. M., et al. (2008), Improvements to NOAA's historical merged land-ocean surface temperature analysis (1880–2006), *J. Clim.*, *21*, 2283–2296, doi:10.1175/2007JCLI2100.1.

Solomon, S., K. H. Rosenlof, R. W. Portmann, J. S. Daniel, S. M Davis, T. J. Sandford, and G.-K. Plattner (2010), Contributions of stratospheric water vapor to decadal changes in the rate of global warming, *Science*, *327*, 1219–1223, doi:10.1126/science.1182488.

Solomon, S., J. S. Daniel, R. R. Neely III, J.-P. Vernier, E. G. Dutton, and L. W. Thomason (2011), The persistently variable "background" stratospheric aerosol layer and global climate change, *Science*, *333*(6044), 866–870, doi:10.1126/science.1206027.

Trenberth, K. E., J. T. Fasullo, G. Branstator, and A. S. Phillips (2014), Seasonal aspects of the recent pause in surface warming, *Nat. Clim. Change*, *4*, 911–916, doi:10.1038/nclimate2341.

Yang, C., B. S. Giese, and L. Wu (2014), Ocean dynamics and tropical Pacific climate change in ocean reanalyses and coupled climate models, *J. Geophys. Res. Oceans*, *119*, 7066–7077, doi:10.1002/2014JC009979.

Wunsch, C., and P. Heimbach (2006), Estimated decadal changes in the North Atlantic Meridional Overturning Circulation and heat flux 1993-2004, *J. Phys. Oceanogr.*, *36*, 2012–2024, doi:10.1175/JPO2957.1.